TU Delft

Delft University of Technology

Document Version
Final published version

Licence
Dutch Copyright Act (Article 25fa)

Citation (APA)
Hadjisotiriou, G., Sass, J., Wapperom, M., Novikov, A., & Voskov, D. (2026). Impact Assessment of Injection Impurities in the SPE11 Geological Carbon Sequestration Benchmark. *SPE Journal*, *31*(5), 3363-3378. https://doi.org/10.2118/223922-PA

Important note
To cite this publication, please use the final published version (if applicable).
Please check the document version above.

Copyright
In case the licence states “Dutch Copyright Act (Article 25fa)”, this publication was made available Green Open Access via the TU Delft Institutional Repository pursuant to Dutch Copyright Act (Article 25fa, the Taverne amendment). This provision does not affect copyright ownership.
Unless copyright is transferred by contract or statute, it remains with the copyright holder.

Sharing and reuse
Other than for strictly personal use, it is not permitted to download, forward or distribute the text or part of it, without the consent of the author(s) and/or copyright holder(s), unless the work is under an open content license such as Creative Commons.

Takedown policy
Please contact us and provide details if you believe this document breaches copyrights.
We will remove access to the work immediately and investigate your claim.

This work is downloaded from Delft University of Technology.

Impact Assessment of Injection Impurities in the SPE11 Geological Carbon Sequestration Benchmark

G. Hadjisotiriou[1]*, J. Sass[2], M. Wapperom[1], A. Novikov[1], and D. Voskov[1,3]

[1]Department of Geoscience & Engineering, TU Delft
[2]Equinor
[3]Department of Earth Science & Engineering, Stanford University

Summary

Accurate reservoir simulation of carbon dioxide (CO_2) sequestration is critical for predicting the distribution of CO_2 during and after injection. Therefore, the 11th SPE Comparative Solution Project (SPE11 CSP) serves as a benchmark for modeling geological carbon storage in an aquifer. In this paper, we present a convergence analysis of the SPE11 benchmark simulation using the Delft Advanced Research Terra Simulator (open-DARTS). In addition, we analyze the effect of trace amounts of impurities in the injection stream. Open-DARTS is an open-source simulation framework designed for both forward and inverse modeling, employing a unified thermal-compositional formulation and operator-based linearization (OBL). In our convergence analysis, the SPE11b (2D-reservoir conditions) starts to converge at a grid resolution of 1,340×240, after which added resolution provides diminishing returns. In addition, the 3D SPE11c benchmark is simulated with 8 million gridblocks. However, 2D results from SPE11b suggest that a greater resolution is required for a truly converged solution. Furthermore, we extend the SPE11b benchmark to include hydrogen sulfide (H_2S) and/or methane (CH_4) as trace impurities in the injection stream. These impurities, which are often present depending on the source of the captured CO_2, are found to influence gas density and CO_2 plume migration. Building upon validated thermodynamic predictions from the hybrid equation of state (hybrid-EOS) model, we simulate the SPE11b benchmark, with a total injection mass fixed at 3,024 kg/d. Impurities are introduced at varying molar fractions to assess their influence on CO_2 solubility, plume migration, and trapping efficiency. While H_2S can inhibit plume migration by increasing the gas density under certain conditions, CH_4 increases plume buoyancy and enhances lateral spreading of the CO_2 plume. Additionally, it is found that CH_4 reduces solubility trapping and reduces storage efficiency of CO_2, whereas H_2S has a negligible impact on solubility trapping.

Introduction

During geological carbon sequestration (GCS), CO_2 is captured from industrial processes, transported, and injected into deep geological formations. These storage complexes typically consist of permeable reservoir rocks overlain by impermeable sealing units. As such, saline aquifers and depleted oil and gas reservoirs are considered the most suitable candidates for GCS. Deep saline aquifers offer the largest proven capacity for CO_2 storage, whereas depleted hydrocarbon reservoirs have a proven ability to retain buoyant fluids over geological timescales, are well-characterized, and often have existing infrastructure in place (Ringrose 2020). Ensuring the safe and permanent sequestration of CO_2 requires the development of robust models that support decision-making by operators and regulators. The 11th SPE Comparative Solution Project (SPE11 CSP) models CO_2 sequestration in a saline aquifer and provides an opportunity to test and improve reservoir simulators while guiding future research in GCS. In this paper, we conduct a resolution study of the SPE11b benchmark using the open-DARTS reservoir simulator. Furthermore, we investigate the effect of adding trace amounts of H_2S and CH_4, two common byproducts of natural gas processing, on the results of the benchmark simulation.

Planning CO_2 storage projects requires an understanding of the storage conditions and fluid flow behavior. To this extent, reservoir simulation is used to predict the migration of CO_2, pressure evolution, and storage capacity of the reservoir. Accurate modeling of CO_2 sequestration necessitates the inclusion of complex physical processes, including gravity, capillarity, diffusion, mechanical dispersion, and multiphase flow. Once injected, CO_2 is retained in the subsurface through a combination of various trapping mechanisms: structural, residual, and solubility trapping. In the shorter time scale, structural and residual trapping mechanisms are expected to dominate, while dissolution trapping occurs over longer time scales (Metz et al. 2005). In structural trapping, the injected CO_2 accumulates under a capillary barrier or impermeable sealing layer. Residual trapping occurs when the CO_2 plume migrates due to buoyancy. In this process, CO_2 at the tail of the plume is immobilized at the pore scale as the wetting phase is imbibed back into the pore space (Krevor et al. 2015). At this point, the CO_2 exists as a series of disconnected ganglia separated by water. During solubility trapping, CO_2 dissolves into the aquifer water. This molecular diffusion process occurs slowly and is enhanced by the convective mixing of the brine and CO_2 (Neufeld et al. 2010). Convective mixing starts at the interface between CO_2 and water. As CO_2 dissolves into the brine, density-driven flow is induced, which in turn increases the dissolution rate. To accurately capture the effect of dissolution trapping, it is necessary to solve the highly nonlinear, coupled system of equations, accounting for all these effects, with both a sufficient resolution and over an extended timescale (Riaz et al. 2006; Pau et al. 2010; Pruess and Nordbotten 2011).

The SPE11 carbon capture and sequestration (CCS) benchmark follows in the footsteps of previous benchmark studies and intercomparisons focused on CCS modeling. Previous intercomparisons by Pruess et al. (2004) have shown a good agreement between solutions obtained with different numerical simulators. The authors attribute discrepancies to differences in the descriptions of fluid properties. However, convective dissolution always introduces a significant challenge to the modeling of long-term CO_2 sequestration at the reservoir

*Corresponding author; email: g.hadjisotiriou@tudelft.nl

Copyright © 2026 Society of Petroleum Engineers

This paper (SPE 223922) was accepted for presentation at the SPE Reservoir Simulation Conference, Galveston, Texas, USA, 25–27 March 2025, and revised for publication. Original manuscript received for review 30 June 2025. Revised manuscript received for review 7 January 2026. Paper peer approved 20 January 2026. This paper is published as part of the 11th Comparative Solution Project Special Issue.

Downloaded from http://onepetro.org/SJ/article-pdf/31/05/3363/5335132/spe-223922-pa.pdf by Bibliotheek TU Delft user on 27 May 2026

scale. Elenius et al. (2015) present for the first time a numerically converged solution for a large-scale plume migration problem encompassing a wide range of dominant physical phenomena, including enhanced CO_2 dissolution. The first benchmark study fully linking experiments and simulations of enhanced dissolution processes was proposed by Nordbotten et al. (2022). Based on typical North Sea reservoirs, a representative heterogeneous geometry was constructed in a meter-scale rig and filled with unconsolidated sands of different types. The forecasts reported by different numerical simulation groups were analyzed in the presence of physical ground truth, provided by a series of repeated experiments on the experimental rig (Flemisch et al. 2024). Several advanced methodologies, including data assimilation based on tracer test results (Tian et al. 2024) and the use of multipoint flux approximation (Wapperom et al. 2024) were reported as the result of this benchmark study.

The SPE11 CSP borrows its geometry from the FluidFlower experiment and offers a baseline for the simulation of CO_2 storage in aquifers (Nordbotten et al. 2024). The reservoir is a heterogeneous reservoir storage complex resembling those found on the Norwegian continental shelf. Three versions of the benchmark are presented in the CSP. The first, 11a is a 2D laboratory-scale geometry at surface conditions. The second, 11b, is geometrically identical to 11a but at reservoir scale and conditions. The third and last, 11b, is a 3D extruded version of 11b that includes an anticline. The aim of the CSP is to provide a reference case for the development of numerical simulation of GCS by comparative study. The SPE11 CSP explicitly specifies all reservoir and fluid properties in the technical problem definition by Nordbotten et al. (2024). In Kovscek et al. (2024), the procedure for upscaling the experimental results of the FluidFlower experiment to storage conditions is described in detail.

In this study, we conduct a convergence analysis of the SPE11b benchmark using open-DARTS, an open-source simulation framework designed for forward and inverse modeling, as well as uncertainty quantification (Voskov et al. 2024). Open-DARTS employs a unified thermal-compositional formulation and OBL (Voskov 2017). This approach allows users to easily adjust the terms of thepartial differential equations and model various complex physical phenomena. Additionally, open-DARTS leverages graphics processing unit (GPU) parallelization, enabling simulations to run close to an order of magnitude faster compared to central processing unit (CPU) implementation (Khait and Voskov 2021). All codes and models included in this manuscript are freely available on the open-DARTS GitLab page: https://gitlab.com/open-darts/darts-models.

Furthermore, the original benchmark is extended to include impurities in the CO_2 injection stream, reflecting realistic field conditions. Carbon capture and storage projects associated with hydrocarbon developments coinject trace amounts of other gases, such as H_2S and CH_4, with CO_2 following degassing. In the case of the Sleipner project, CO_2 is coinjected with a 0.5–2% fraction of CH_4 in an adjacent aquifer (Eiken et al. 2011). Additionally, in the Weyburn project, H_2S (sour gas) is coinjected with CO_2 (Whittaker et al. 2004). Depending on temperature and pressure conditions, the inclusion of such impurities can significantly affect various operational parameters. In particular, impurities alter phase behavior, fluid properties, and CO_2 trapping mechanisms, ultimately reducing overall CO_2 storage capacity. These changes, in turn, impact long-term storage security and project economics because the cost of separating impurities must be weighed against the loss of CO_2 storage capacity, and by extension, project revenue. If the loss is considerable, it may be favorable to instead remove CH_4 and H_2S from the injection stream to an extent.

The paper is structured as follows. We begin with a brief description of the governing equations and thermodynamic properties, highlighting the exact property correlations used and noting where they differ from those prescribed in the benchmark. We then describe the reservoir and the initial and boundary conditions of the SPE11 benchmark. Next, we present a convergence study for the SPE11b reservoir, followed by a comparison of the converged solution with the results of the SPE11c simulation. This comparison provides a baseline for evaluating the results of ternary simulations that include impurities. Subsequently, we present the results of the SPE11b model with impurities in the CO_2 stream. Finally, we conclude with lessons learned and suggestions for future work.

The SPE11 CSP

What follows is an abbreviated description of the SPE11 CSP. For a complete description of the CSP, please refer to the official technical description by Nordbotten et al. (2024). As CO_2 is frequently injected at lower temperatures than the reservoir, a thermo-compositional formulation is used. In DARTS, the advective-diffusive multiphase multicomponent formulation is used (Lyu and Voskov 2023). The mass conservation equation for component c is written as

$$\frac{\partial}{\partial t}\left(\phi \sum_{j=1}^{n_p} \rho_j^m s_j x_{cj}\right) + \nabla \cdot \left(\sum_{j=1}^{n_p} \left(x_{cj}\rho_j^m \mathbf{u}_j + \mathbf{J}_{cj}\right)\right) = 0, \quad c = 1, ..., n_c, \tag{1}$$

where ϕ is the porosity, s_j is the phase saturation, ρ_j^m is the molar phase density, and x_{cj} is the molar fraction of component c in phase j.

Additionally, the thermal equation for multiphase flow accounts for advective and conductive heat flow and contains contributions from both fluid and rock:

$$\frac{\partial}{\partial t}\left(\phi \sum_{j=1}^{n_p} \rho_j^m s_j U_j + (1-\phi)U_r\right) + \nabla \cdot \left(\sum_{j=1}^{n_p} h_j \rho_j^m \boldsymbol{u}_j + \kappa \nabla T\right) = 0, \tag{2}$$

where U_j is the specific internal energy of phase j, U_r is the rock specific internal energy, κ is the effective heat conductivity, h_j is the phase enthalpy, and T is the temperature. The phase velocity $\mathbf{u}_j$ follows Darcy's law for multiphase flow,

$$\mathbf{u}_j = -\mathbf{K}\frac{k_{rj}}{\mu_j}(\nabla p_j - \rho_j^m M_j g \nabla z), \tag{3}$$

where $\mathbf{K}$ is the permeability tensor, k_{rj} is the relative phase permeability, μ_j is the phase viscosity, p_j is the phase pressure, M_j is the phase molar weight, g is the gravitational acceleration, and z is the depth.

The diffusive flux $\mathbf{J}_{cj}$ of component c in phase j is described by Fick's law as

$$\mathbf{J}_{cj} = -\rho_j^m(\phi s_j D_{cj} + E|\mathbf{u}_j|)\nabla x_{cj}, \tag{4}$$

where D_{cj} is the diffusion coefficient of component c in phase j and E is the dispersivity coefficient (equal for all components in all phases). In this formulation, dispersion is dependent on Darcy velocity. The velocity vector is reconstructed at cell centers using a

Downloaded from http://onepetro.org/SJ/article-pdf/31/05/3363/5335132/spe-223922-pa.pdf by Bibliotheek TU Delft user on 27 May 2026

least-squares solution of fluxes across all cells' interfaces, then averaged between neighboring cells, and explicitly incorporated into the numerical approximation of the dispersion term (Novikov and Voskov 2025).

Thermodynamics and Physical Properties. A negative flash procedure with successive substitution is used for resolving thermodynamic equilibrium calculations (Michelsen 1982; Whitson and Michelsen 1989). The fugacities of the vapor phase are evaluated using a cubic EOS and the fugacities of the water phase are calculated using an activity model based on Henry's constants (Peng and Robinson 1976; Ziabakhsh-Ganji and Kooi 2012). This hybrid-model approach enables accurate thermodynamic representation of the water phase while preserving the computational simplicity and ease of cubic EOS flash calculations (Wapperom 2026).

The property correlations for SPE11 and open-DARTS are summarized in **Table 1**. The properties of pure phases of the SPE11 CSP are defined following the NIST database (Lemmon et al. 2023). Wapperom et al. (2024) compared the results of our modeling approach with those of NIST and found good agreement. **Fig. 1** presents the results of the models used in this work, verified against various data sets available in the literature. The considered properties are highly dependent on pressure and temperature, except for the dissolved H_2O in the CO_2-rich phase at field conditions. At elevated pressures, changes in pressure exert minimal influence on solubility when the CO_2 is in a dense phase. Conversely, at low pressures, CO_2 in a vaporous state results in a greater concentration of H_2O within the CO_2 phase. As pressure increases, the transition from the vapor phase to the dense phase results in a pronounced decline in solubility.

Properties	SPE11	open-DARTS
CO_2 density (kg/m^3)	Lemmon et al. (2023)	Peng and Robinson (1976)
H_2O density (kg/m^3)	Garcia (2001)	Garcia (2001)
CO_2viscosity (cp)	Lemmon et al. (2023)	Fenghour et al. (1998)
H_2O viscosity (cp)	Lemmon et al. (2023)	Islam and Carlson (2012)
CO_2 enthalpy (kJ/kmol)	Lemmon et al. (2023)	Peng and Robinson (1976)
H_2O enthalpy (kJ/kmol)	Lemmon et al. (2023)	Ziabakhsh-Ganji and Kooi (2012)
Mutual solubilities	Spycher et al. (2003)	Wapperom (2026)
Gas diffusion coefficient (m^2/s)		2×10^{-8}
Water diffusion coefficient (m^2/s)		1×10^{-9}

Table 1—Fluid properties of 11b and 11c.

In addition, the capillary pressure p_c, defining the pressure drop between wetting and nonwetting phases, is governed by the following relationship:

$$p_c(s_w) = \mathrm{p_{cap,max}} \cdot \mathrm{erf}\left((\mathrm{p_{entry}}(s_{\mathrm{w,n}})^{-1/\mathrm{c_2}}/\mathrm{p_{cap,max}})(\sqrt{\pi}/2)\right), \quad (5)$$

where $\mathrm{p_{cap,max}}$ is the maximum capillary pressure, $\mathrm{p_{entry}}$ is the entry pressure, and $\mathrm{c_2}$ is an empirical parameter. The exact values of these properties are provided in **Table 2**.

Property	Symbol	Unit	Value
Dispersivity	E	m	10
Immobile gas saturation	$s_{n,\mathrm{imm}}$		0.1
Max. capillary pressure	$\mathrm{p_{cap,max}}$	Pa	3×10^7
Shape exponent capillary pressure	$\mathrm{c_2}$		1.5
Rock specific heat capacity	C_s	kJ/kg/K	8.5×10^{-1}
Rock density	ρ_S	kg/m^3	2,500
Shape exponents relative permeability	$\mathrm{c_1}$		1.5
Normalized saturations	$s_{j,n}$		$\max\left(\frac{s_j - s_{j,\mathrm{imm}}}{1 - s_{j,\mathrm{imm}}}, 0\right)$
Relative permeability	k_{rj}		$(s_{j,n})^{\mathrm{c_1}}$
Relative permeability endpoints			1.0
Entry pressure	$\mathrm{p_{entry}}$	bar	$\sqrt{\phi/k_x}6.12\times10^{-3}$ Nm^{-1}

Table 2—Porous media properties.

Reservoir. Seven different facies are defined in both the 11b and 11c reservoir models. Facies 1 represents the storage complex and functions as a capillary barrier to migrating CO_2. Facies 2 through 5 consist of permeable reservoir sands, while Facies 6 corresponds to fault infill. Finally, Facies 7 forms an impermeable barrier. The spatial distribution of facies for the 11b model is shown in **Fig. 2**. The 11c model is a 3D extruded version of the planar 11b model, is tilted, and also includes an anticline. Note that in SPE11, the reservoir geometry defines the z-axis at the base of the reservoir. Facies properties are identical for both models and are listed in **Table 3**. The vertical permeability of each of the facies is one-tenth of its horizontal permeability. Model geometries of the three SPE11 variants are

Downloaded from http://onepetro.org/SJ/article-pdf/31/05/3363/5335132/spe-223922-pa.pdf by Bibliotheek TU Delft user on 27 May 2026

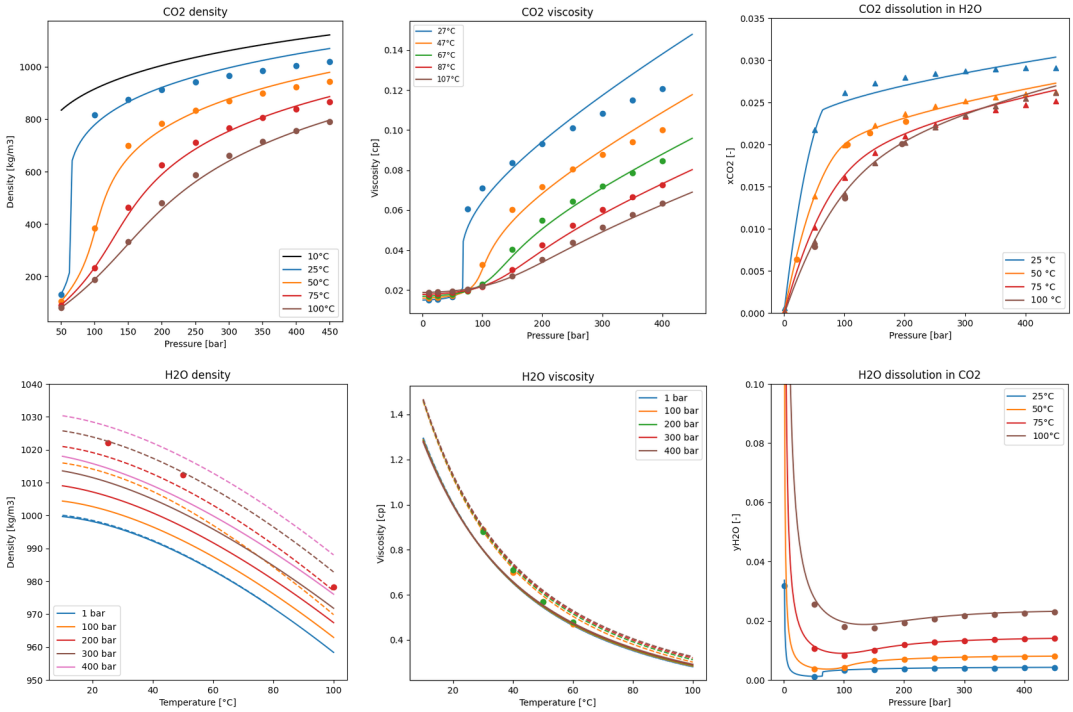


Fig. 1—Fluid properties at various reservoir conditions used within DARTS for simulation. The critical point of CO_2 is approximately 31 °C and 74 bar. All properties are highly dependent on pressure and temperature except for dissolved H_2O in the CO_2-rich phase at field conditions. At high pressures, changes in pressure have little effect on solubility. The transitions between vapor and dense phase CO_2 are more gradual at high temperatures. From top left to bottom right: CO_2 phase density (Lemmon et al. 2023) (●); CO_2 phase viscosity (Fenghour et al. 1998) (●); CO_2 dissolutionn in H_2O (Spycher et al. 2003) (△) and (Koschel et al. 2006) (●); H_2O density, solid curves for pure phase, dashed for saturated brine (Hnedkovsky et al. 1996) (●); H_2O viscosity, solid curves for pure phase, dashed curves for saturated brine (Bando et al. 2004) (●); H_2O dissolution in CO_2, vaporization of water in the CO -phase (Spycher et al. 2003) (●).

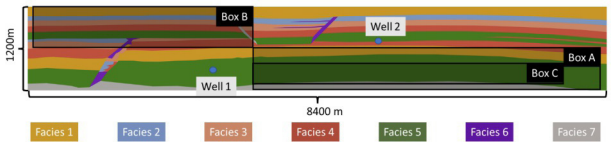


Fig. 2—SPE11b, reservoir with corresponding reporting boxes and well locations (Nordbotten et al. 2024).

hosted on the GitHub repository: https://github.com/Simulation-Benchmarks/11thSPE-CSP. Reservoir geometries are provided in the GMSH geometry format and are available in the SPE11 repository. In our model, the geometry of the FluidFlower model is converted to the reservoir scale following the SPE11's description. For all simulations, a structured mesh is constructed and populated according to the facies descriptions. A detailed comparison between the structured and unstructured grid approaches for the original FluidFlower formulation is available in Wapperom et al. (2024).

Facies No.	Permeability, k_x (md)	Porosity, ϕ	$s_{w,\mathrm{imm}}$	Rock Heat Conductivity, κ_s, $\left(\mathrm{W\ m^{-1}K^{-1}}\right)$
1	0.101	0.10	0.32	1.90
2	101	0.20	0.14	1.25
3	202	0.20	0.12	1.25
4	507	0.20	0.12	1.25
5	1,013	0.25	0.12	0.92
6	2,027	0.35	0.10	0.26
7	0	0	N/A	2.00

Table 3—Facies properties of 11b and 11c.

Downloaded from http://onepetro.org/SJ/article-pdf/31/05/3363/5335132/spe-223922-pa.pdf by Bibliotheek TU Delft user on 27 May 2026

Initial and Boundary Conditions. In both the SPE11b and 11c models, temperatures are fixed at the top and bottom boundaries, while all boundaries are impermeable and the boundary volumes are increased to $5 \times 10^4 \Delta z$. No CO_2 is present in the system before injection. A geothermal gradient of 25°C/km is applied along with a temperature of 70°C maintained at the bottom boundary. The initial reservoir pressure is hydrostatic and defined as

$$p_{w,initial} = 3 \times 10^7 \text{Pa} - g \int_{300\text{m}}^{z} \rho_w(p, T) dz, \tag{6}$$

where ρ_w is the water phase density. The model undergoes an equilibration step lasting 1,000 years before injection, with $t = 0$ years defined as the start of injection. Both the 11b and 11c models include two injection wells. In Model 11b, Well 1 is located at (2,700; 300) and Well 2 is located at (5,100; 1,100). For Model 11c, the wells are horizontal. Well 1 perforates the reservoir between points (2,700; 1,000; 300) and (2,700; 4,000; 300) and Well 2 perforates the reservoir between points (5,100; 1,000; 700) and (5,100; 4,000; 700). In both models, injection starts in Well 1 at $t = 0$ years and continues until $t = 50$ years. Well 2 starts injection at $t = 25$ years, lasting until $t = 50$ years. In the post-injection period, the simulation continues until $t = 1{,}000$ years. In both wells, CO_2 is injected at 10°C. In 11b, the injection rate is equal to 3,024 kg/d and in 11c, it is equal to 50 kg/s.

Solution Strategy. A finite-volume discretization is employed, using the backward-Euler scheme in time and two-point flux approximation with single-point upstream weighting in space. OBL is used to manage the computational cost associated with property evaluation and Jacobian assembly. In OBL, the governing equations are represented through state-dependent and spatial operators. State-dependent operators aggregate variables that depend on the physical state into a single term (i.e., operator). The state operators are resolved on a uniform mesh introduced in the physical space. While the operators undergo exact evaluation at the nodes of this mesh, multilinear interpolation ensures a continuous representation of the operators between the nodes. The mesh resolution provides a key control over the nonlinearity of the problem, simulation performance, and robustness of the simulation (Khait and Voskov 2017). Therefore, to accurately capture multiphase flow in the presence of capillarity and buoyancy, a resolution of 100 points is used for pressure and 1,000 points for composition space, which is sufficient for included physics (Lyu et al. 2021).

Results

The SPE11 CSP data set includes both time series and spatial data. Note that here the spatial maps are shown in their native resolution and are not projected on the SPE11 reporting grid. Time series data include pressure at two observation points (S1 and S2), convective mixing M in Box C and the total mass of CO_2. The mass of CO_2 contained in Boxes A and B, as well as in the seals, is reported. The location of the boxes with respect to the injection wells is visualized in **Fig. 2**. Convective mixing is quantified by the integral of normalized concentrations:

$$M = \int \nabla \left| \frac{X^w_{\text{CO}_2}}{X^w_{\text{CO}_2,\text{max}}} \right| dV, \tag{7}$$

where $X^w_{\text{CO}_2}$ is the mass fraction of CO_2 in the water phase and $X^w_{\text{CO}_2,\text{max}}$ is the solubility limit of CO_2 in water defined at the mean temperature and pressure in Box C.

SPE11b. This study compares the simulation results of the SPE11b model obtained using multiple grid resolutions on a structured grid. The exact grid specifications are reported in **Table 4**. The models with roughly 50,000 and 100,000 gridblocks are considered as low-resolution, whereas the models with just about 300,000 and 600,000 gridblocks are considered high-resolution models. The spatial solutions are shown in **Figs. 3 and 4**. Injection begins in Well 1. Initially, the colder injected gaseous CO_2 sinks downward due to its higher density compared to the surrounding reservoir water. However, as the CO_2 equilibrates with the reservoir temperature, it migrates upward due to buoyancy. Subsequently, the majority of CO_2 accumulates beneath the capillary barrier and begins lateral migration, while a portion migrates via the adjacent fault to the upper sand units.

No. Gridblocks	$n_x \times n_z$	dx × dz	Runtime (GPU) (hours)
52,500	525 × 100	16 m × 12 m	1
100,800	840 × 120	10 m × 10 m	2
321,600	1,340 × 240	6.27 m × 5 m	7
604,800	1,680 × 360	5.0 m × 3.3 m	11

Table 4—Grid specifications.

Downloaded from http://onepetro.org/SJ/article-pdf/31/05/3363/5335132/spe-223922-pa.pdf by Bibliotheek TU Delft user on 27 May 2026

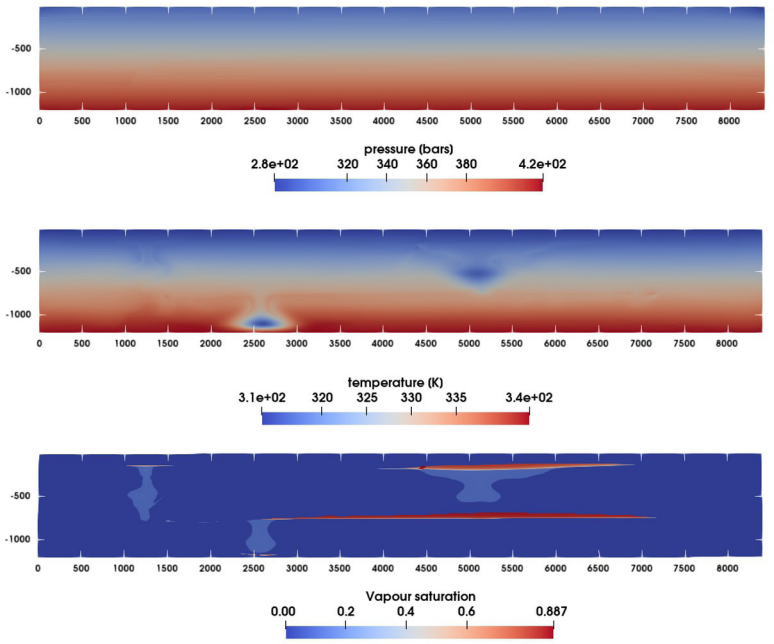


Fig. 3—SPE11b; pressure, temperature, and gas saturation at Year 300; the model has a resolution of 600,000 gridblocks.

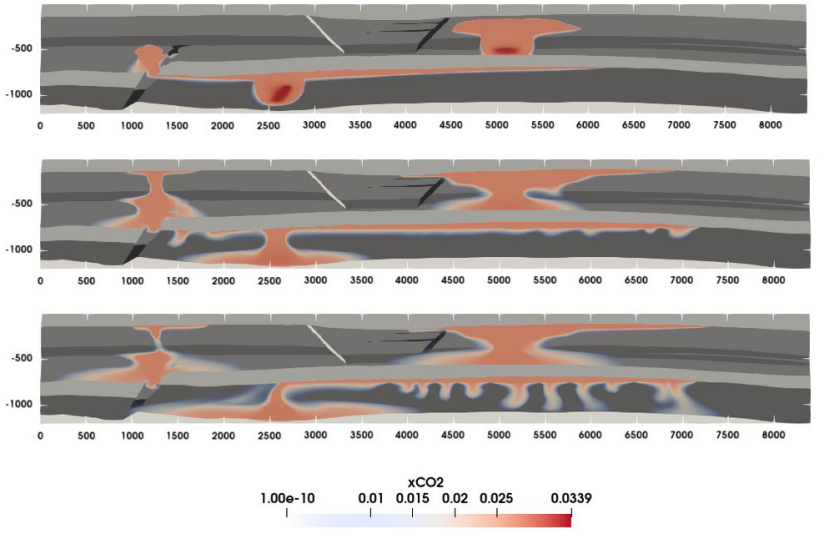


Fig. 4—SPE11b, CO_2 molar fraction in liquid phase post-injection at Years 50, 300, and 600 (from top to bottom). The model has a resolution of 600,000 gridblocks.

As the CO_2 plume migrates upward to Box B, residual trapping takes place. In Box A, two principal processes are observed: First, the CO_2 diffuses into the capillary barrier; second, the CO_2 starts to dissolve into the reservoir water. This dissolution alters the water's density, making it heavier, inducing instabilities, and leading to the formation of finger-like patterns of CO_2-saturated water. These fingers enhance the dissolution process by increasing the surface area for interaction between CO_2 and water, thereby accelerating mixing and promoting more secure storage of CO_2.

Several observations can be derived from **Fig. 5**. Convective mixing increases as CO_2 dissolves into the aquifer water. The onset of dissolution can be identified as an inflection point in the curve for convective mixing and occurs in Year 300. By Year 600, the amount of convective mixing decreases as more of the water column is in contact with CO_2 and density contrasts decrease. Post-injection CO_2 begins to diffuse into the sealing unit at an increasing rate.

In Box A, **Fig. 6**, minor differences are observed in the amounts of dissolved and mobile CO_2 across varying resolutions. Around Year 300, the amount of mobile CO_2 begins decreasing, coinciding with the onset of enhanced dissolution and an increased dissolution rate. Nevertheless, the higher-resolution models exhibit less immobilized CO_2 compared to the lower-resolution models, which is consistent with results present in Wapperom et al. (2024). Furthermore, the final amount of CO_2 accumulating in the seal increases with finer resolution.

CO_2 enters Box B at approximately Year 20. In Box B, **Fig. 7**, the amount of mobile CO_2 consistently increases with finer resolutions, whereas it remains virtually unchanged for the 300,000 and 600,000 gridblock models. Similarly, the higher-resolution models also exhibit greater amounts of CO_2 in Seal B and higher levels of dissolved CO_2, indicating a strong resolution-dependent trend

Downloaded from http://onepetro.org/SJ/article-pdf/31/05/3363/5335132/spe-223922-pa.pdf by Bibliotheek TU Delft user on 27 May 2026

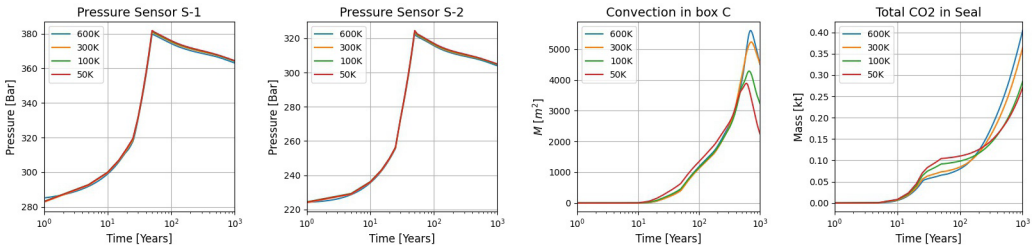


Fig. 5—SPE11b time-series data.

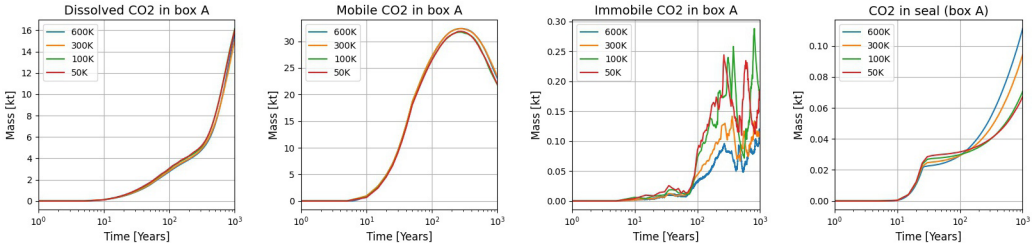


Fig. 6—SPE11b, Box A—bottom left (3,300; 0), top right (8,300; 600).

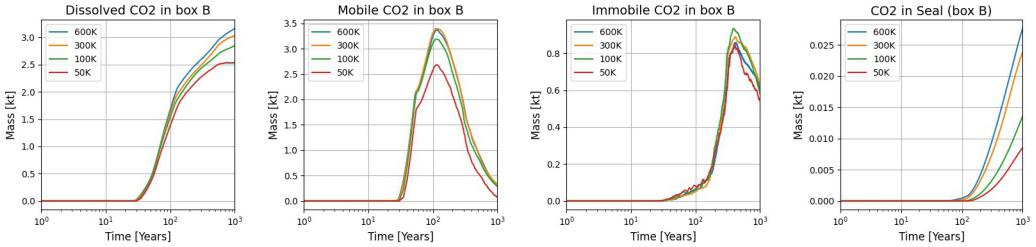


Fig. 7—SPE11b, Box B—bottom left (100; 600), top right (3,300; 1200).

across all models. No density-driven fingering is observed in Box B, and greater amounts of CO_2 are immobilized compared to Box A.

Fig. 8 shows the relative proportion of dissolved, mobile, and immobile CO_2 in each of the boxes which can be viewed as analogs for solubility, structural, and capillary trapped CO_2. Evidently, in Box A, no capillary trapping takes place, and the CO_2 is either structurally trapped or dissolved into the water. In Box B, located in the upper sand unit, CO_2 travels further and is residually trapped.

It is important to consider the effects of including dispersion in the advection/diffusion equation. Dispersion accounts for microscopic variations of component concentrations and velocities by adding a linear term to Fick's law that scales with the phase velocities (Bear and Cheng 2010). Dispersion increases the component fluxes and therefore acts as an additional spreading mechanism for CO_2. In **Fig. 9**, we compare the total mass of CO_2 in the SPE11b benchmark with and without dispersion enabled. Despite the marked decrease in velocity at the post-injection period, the spread of CO_2 is visibly enhanced when dispersion is enabled. The model with dispersion enabled exhibits a wavelength between $x = 4{,}000$ m and $x = 7{,}000$ m of approximately 300 m, therefore indicating that the dispersive fluxes are orders of magnitude greater than the diffusive fluxes and that the critical wavelength of the model with dispersion is much greater than what the diffusion coefficient initially suggests. In Year 500, the mean aqueous phase velocity is equal to 0.00026 m/d . Assuming the critical wavelength in Facies 5 without dispersion is between 0.1 m and 1 m, the adjusted critical wavelength with dispersion lies between 3.1 m and 31 m.

SPE11c. In addition, the full SPE11c model is run using the GPU version of DARTS. In this run, we neglect dispersion. The model consists of $nx = 840$, $ny = 250$, $nz = 120$ blocks per dimension, corresponding to 8,041,864 active reservoir blocks. The 3D representation with two profiles across the model at $x = 2{,}700$ and $x = 6{,}000$ are shown in **Fig. 10**, depicting the fraction of CO_2 in the liquid phase at 600 years of simulation. The results at three different timesteps for cross-sections along the model at $y = 2{,}600$ are presented in **Fig. 11**.

Several conclusions can be derived from the comparison of **Figs. 4 and 11**. The results indicate that CO_2 does not spill through the left-most fault, which is attributed to the dipping of the reservoir. Moreover, it is quite obvious that the current resolution of the SPE11c model is insufficient to accurately capture the dynamics of enhanced dissolution, as the simulation does not resolve the characteristic length of fingers and their general dynamics.

SPE11b with Impurities. In this section, we study the effect of H_2S and CH_4 impurities in the injection stream of the SPE11b benchmark. We do not treat the SPE11c model with impurities as the converged benchmark without impurities is already computationally expensive. Hydrodynamic dispersion is excluded from these models for two reasons. First, the calculation of velocities at every timestep is computationally expensive. Second, buoyancy of the CO_2 plume is relatively insensitive to molecular diffusion and dispersion. Moreover,

Downloaded from http://onepetro.org/SJ/article-pdf/31/05/3363/5335132/spe-223922-pa.pdf by Bibliotheek TU Delft user on 27 May 2026

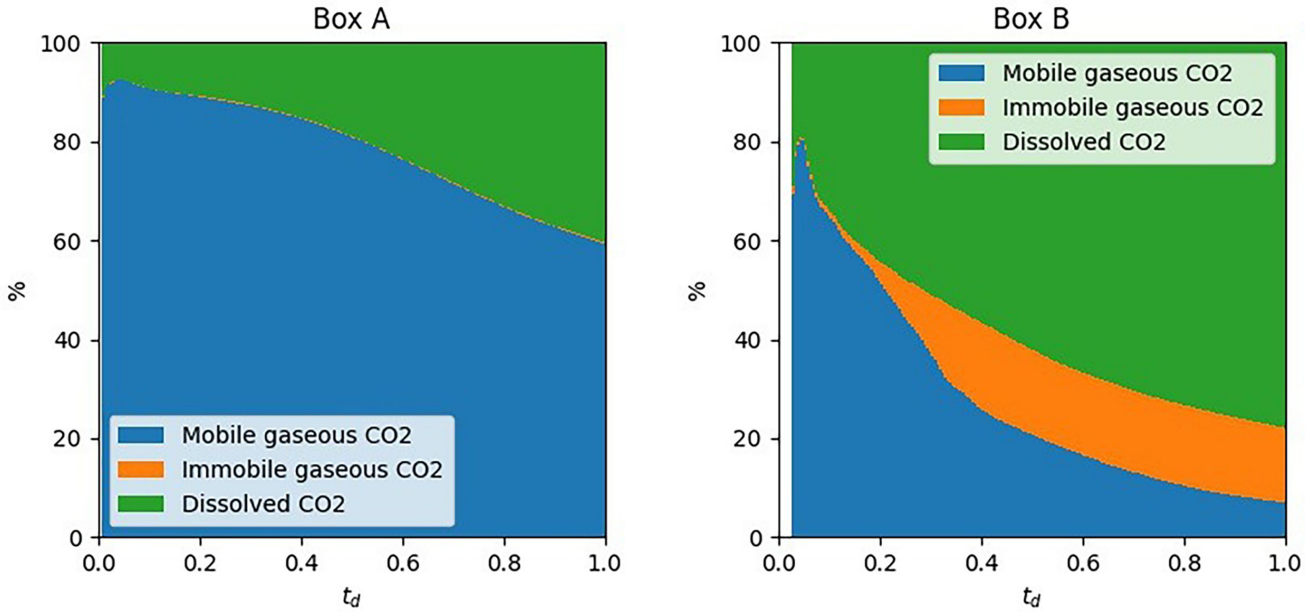


Fig. 8—SPE11b, trapping mechanisms in Boxes A and B.

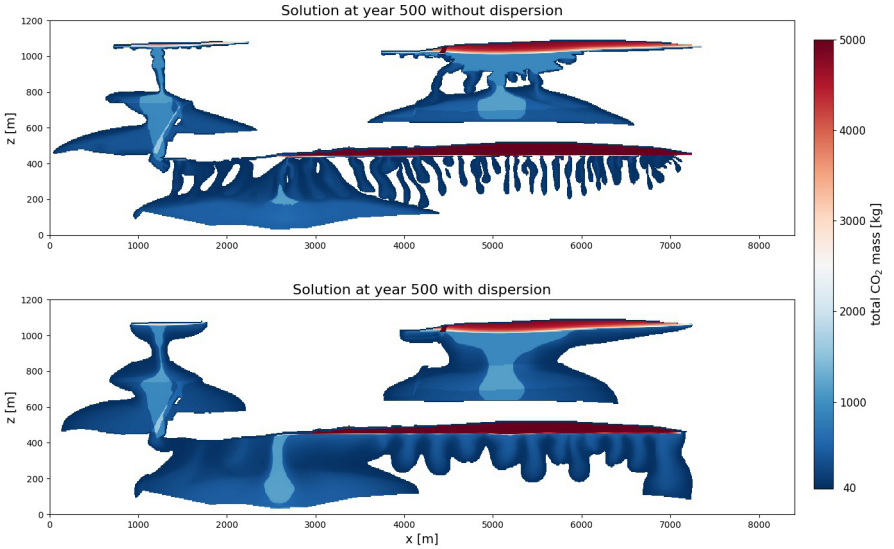


Fig. 9—SPE11b, total mass of CO_2 with (bottom) and without (top) dispersion.

the SPE11b reporting grid resolution is used since it is a good reference resolution that was used by the majority of CSP submissions. The property relations and injection schedules are identical to those used for the benchmark and are listed in **Table 1**. In each of the cases, the injection rates are specified so that the total mass injected per well remains equal to 3,024 kg/d.

Accurate modeling of phase behavior is a prerequisite for modeling CO_2 mixtures in aqueous solutions. Arguably, for these water-containing mixtures, a thermodynamic modeling approach that explicitly accounts for cross-association between water and other species is arguably necessary. This is especially true in the case of H_2S-rich compositions that fall within the three-phase liquid/liquid/vapor region (Li and Firoozabadi 2009). However, for trace amounts of H_2S injected, the effects of cross-association are expected to be minimal. Furthermore, Wapperom (2026) validated the results of the cubic-EOS-based hybrid-EOS model against various experimental data sets of CH_4– and H_2S–CO_2 mixtures, and experimental data points from Huang et al. (1985) for a quaternary mixture containing CH_4, CO_2, H_2S, and H_2O are compared to the results of DARTS-flash in **Tables B-1 and B-2** in Appendix B. Since only small amounts of H_2S are injected, we only compare with Mixture 1 of Huang et al. (1985), as this mixture most closely represents the injection/storage compositions presented in the following models.

The inclusion of CH_4 impurities in CO_2 gas mixtures decreases the solubility of CO_2 in water (Hajiw et al. 2018). Due to the hazardous nature of H_2S, limited experimental data exist for H_2S mixtures at reservoir conditions. However, available measurements show that the solubility of CO_2 decreases in the presence of H_2S (Savary et al. 2012). Additionally, field observations, laboratory experiments (Bachu and Bennion 2009), and numerical simulations (Zhang et al. 2011) show that the leading edge of the gas plume contains higher concentrations of CO_2. This chromatographic partitioning arises from the higher solubility of H_2S in water and its distinct displacement

Downloaded from http://onepetro.org/SJ/article-pdf/31/05/3363/5335132/spe-223922-pa.pdf by Bibliotheek TU Delft user on 27 May 2026

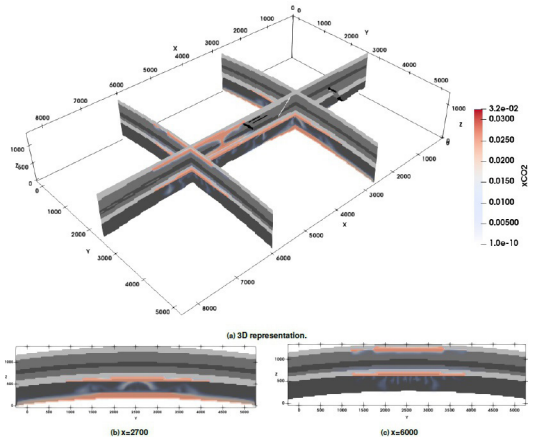


Fig. 10—SPE11c, 8 million gridblocks model at Year 600 with two cross-sections across the model.

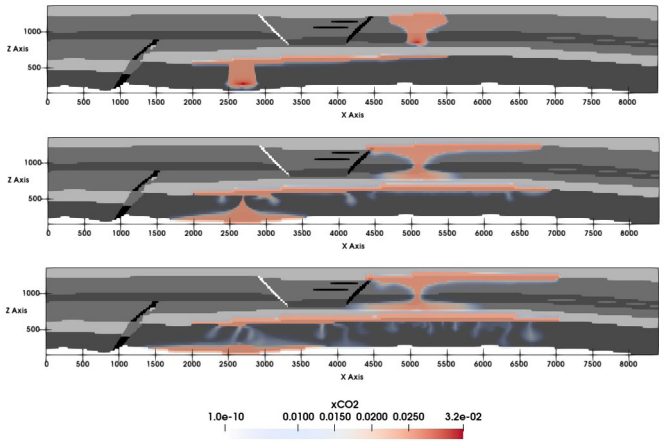


Fig. 11—SPE11c, CO_2 aqueous molar fraction of the SPE11c model at y = 2,600 in Years 50, 300, and 600 (from top to bottom).

characteristics near the leading shock front (Orr 2007). On the other hand, additional experiments and simulations indicate that the impact of H_2S on solubility trapping of CO_2 is negligible (Li et al. 2017; Gamal Rezk et al. 2023; Zaidin et al. 2024).

The effect of impurities on the phase density and buoyancy of the gas plume is of particular interest, as these properties strongly influence its lateral and vertical spread of CO_2. Open-DARTS uses an EOS-based density formulation in which phase density is calculated as the sum product of the phase molar fractions and the component molar masses divided by the molar volume: $\sum \frac{x_c M_c}{V}$. The impact of CH_4 and H_2S impurities on gas density in CO_2–CH_4 and CO_2–H_2S mixtures is illustrated in **Table 5**. CH_4 consistently reduces gas density more than H_2S, as the latter tends to liquefy under reservoir conditions, while CH_4 remains noncondensable. Additionally, the difference in molar density between CO_2 and CH_4 is greater than that between CO_2 and H_2S. Under high-temperature, low-pressure storage conditions, it is found that for an H_2O-rich mixture of CO_2 and H_2S, the gas density relative to a binary CO_2–H_2O mixture increases. If this is the case, it could potentially result in a delay of the buoyant rise and spread of the CO_2 plume. This aligns with findings from Li et al. (2017) and Gamal Rezk et al. (2023), who report reduced lateral migration of CO_2 that they attribute to the higher density and decreased buoyancy of the gas plume.

			CH_4 mixture		H_2S mixture	
P (bar)	T (°C)	Composition (CH_4/H_2S, CO_2, H_2O)	ρ_v (kg/m^3)	ρ_{Aq} (kg/m^3)	ρ_v (kg/m^3)	ρ_{Aq} (kg/m^3)
220	10	(0.00, 1.00, 0.00)	1,019	0	1,019	0
		(0.05, 0.95, 0.00)	960	0	1,010	0
		(0.05, 0.05, 0.90)	418	1,017	961	1,018
220	60	(0.00, 1.00, 0.00)	728	0	728	0
		(0.05, 0.95, 0.00)	671	0	725	0
		(0.05, 0.05, 0.90)	302	999	749	1,000
300	10	(0.00, 1.00, 0.00)	1,063	0	1,063	0

Table 5—Density of ternary mixtures vs. pure CO_2.

Downloaded from http://onepetro.org/SJ/article-pdf/31/05/3363/5335132/spe-223922-pa.pdf by Bibliotheek TU Delft user on 27 May 2026

			CH_4 mixture		H_2S mixture	
P (bar)	T (°C)	Composition (CH_4/H_2S, CO_2, H_2O)	ρ_v (kg/m^3)	ρ_{Aq} (kg/m^3)	ρ_v (kg/m^3)	ρ_{Aq} (kg/m^3)
		(0.05, 0.95, 0.00)	1,007	0	1,053	0
		(0.05, 0.05, 0.90)	491	1,020	991	1,022
300	60	(0.00, 1.00, 0.00)	829	0	829	0
		(0.05, 0.95, 0.00)	777	0	824	0
		(0.05, 0.05, 0.90)	385	1,002	817	1,004

Table 5 (continued)—Density of ternary mixtures vs. pure CO_2.

In **Fig. 12**, H_2S is introduced as an impurity in the SPE11b model, with a combined injection of 120 kgH_2S/d and 2,904 kgCO_2/d. Evidently, the overall flow solution remains unchanged, suggesting that trace amounts will not compromise storage security. Chromatographic partitioning is observed at the leading edge of the gas plume, as the mole fraction of H_2S in the aqueous phase is lower at the front of the gas front compared to CO_2.

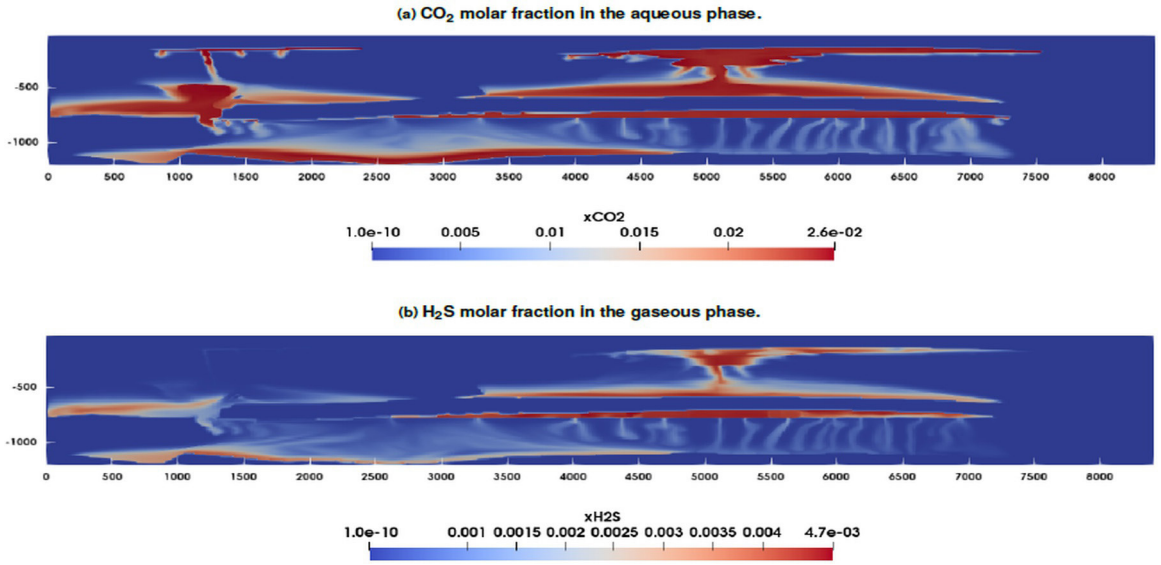


Fig. 12—SPE11b, simulation results of 5 mol% H_2S coinjection. Corresponding to an injection rate of 120 kgH_2S/d and 2,904 kgCO_2/d.

In **Fig. 13**, 58 kgCH_4/d and 2,966 kgCO_2/d are injected. CH_4 exhibits significantly lower solubility in aquifer water compared to CO_2, thereby increasing the overall buoyancy of the gas mixture, heightening storage risks, and potentially reducing the effectiveness of residual trapping. Furthermore, due to its lower solubility, CH_4 tends to form a CH_4-rich gas bank ahead of the migrating CO_2 front. This early migration behavior may serve as an early warning indicator, allowing for preemptive detection of gas movement ahead of the main CO_2 plume. Additionally, it is observed that the CO_2 plume migrates farther laterally in the CH_4 case compared to the H_2S and pure CO_2 models. This is attributed to the increased buoyancy of the plume due to CH_4.

To further illustrate the effect on plume migration, chromatographic partitioning of H_2S and CH_4 bank formation, the SPE11b benchmark is homogenized to Facies 5 and Well 1 is set to inject 3,024 kg/d, with 5 mol% impurities, continuously for 50 years. In **Fig. 14**, the overall molar fraction of CO_2 is depicted alongside the molar gas fraction and gas saturation at the upper boundary of the reservoir. In the case of CH_4 coinjection, the vertical gas column rising from the injection well is slightly less wide and reaches the top of the reservoir quicker and spreads laterally at the top considerably faster than the case of pure CO_2 injection. In Year 70, the gas reaches approximately 1,000 m farther into the reservoir. Additionally, an elevated CH_4 concentration is observed along the gas column and at the leading edge of the gas plume. In the context of H_2S coinjection, the impact on plume migration is found to be negligible. Furthermore, chromatographic partitioning of CO_2 and H_2S is observed.

In the case of H_2S injection, the change in dissolved CO_2 is negligible, as shown in **Fig. 15**, where we plot the ratio of dissolved CO_2 mass to total CO_2 mass across the domain and within Boxes A and B. In contrast, CH_4 significantly reduces CO_2 dissolution in water as even a 5 mol% addition results in a marked reduction in solubility trapping.

Discussion

The following section will provide a detailed discussion of the resolution and impurities study. In our convergence study, the finite volume method is used. The finite volume method is the industry standard and method of choice for the CSP due to its robustness for large simulations. However, higher-order finite element methods are promising since they can capture the convective mixing process with lower resolution grids. The results indicate that the amount of CO_2 in the sealing units is highly dependent on the vertical resolution of the model, while CO_2 plume dynamics remain consistent across different resolutions. Earlier experiences from the FluidFlower experiment, from which the SPE11 model borrows its geometry, and an extensive analysis of various grid types and flux approximation schemes for the SPE11 model conclude that Cartesian grids with two-point flux approximation (TPFA) discretizations are a suitable choice for

Downloaded from http://onepetro.org/SJ/article-pdf/31/05/3363/5335132/spe-223922-pa.pdf by Bibliotheek TU Delft user on 27 May 2026

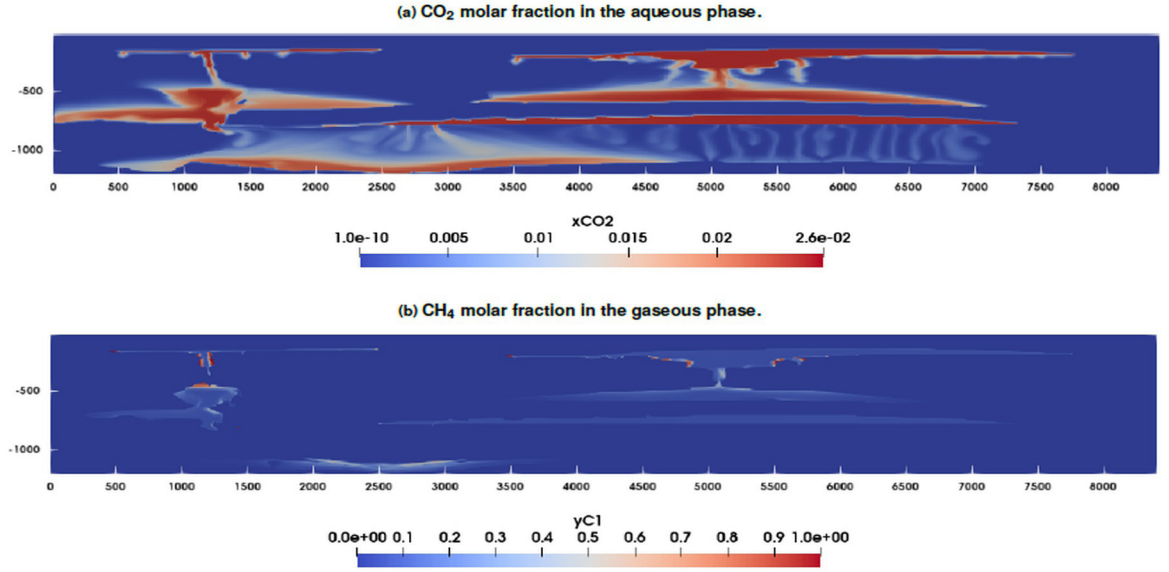


Fig. 13—SPE11b, simulation results of 5 mol% CH_4 coinjection. Corresponding to an injection rate of 58 $kgCH_4/d$ and 2,966 $kgCO_2/d$.

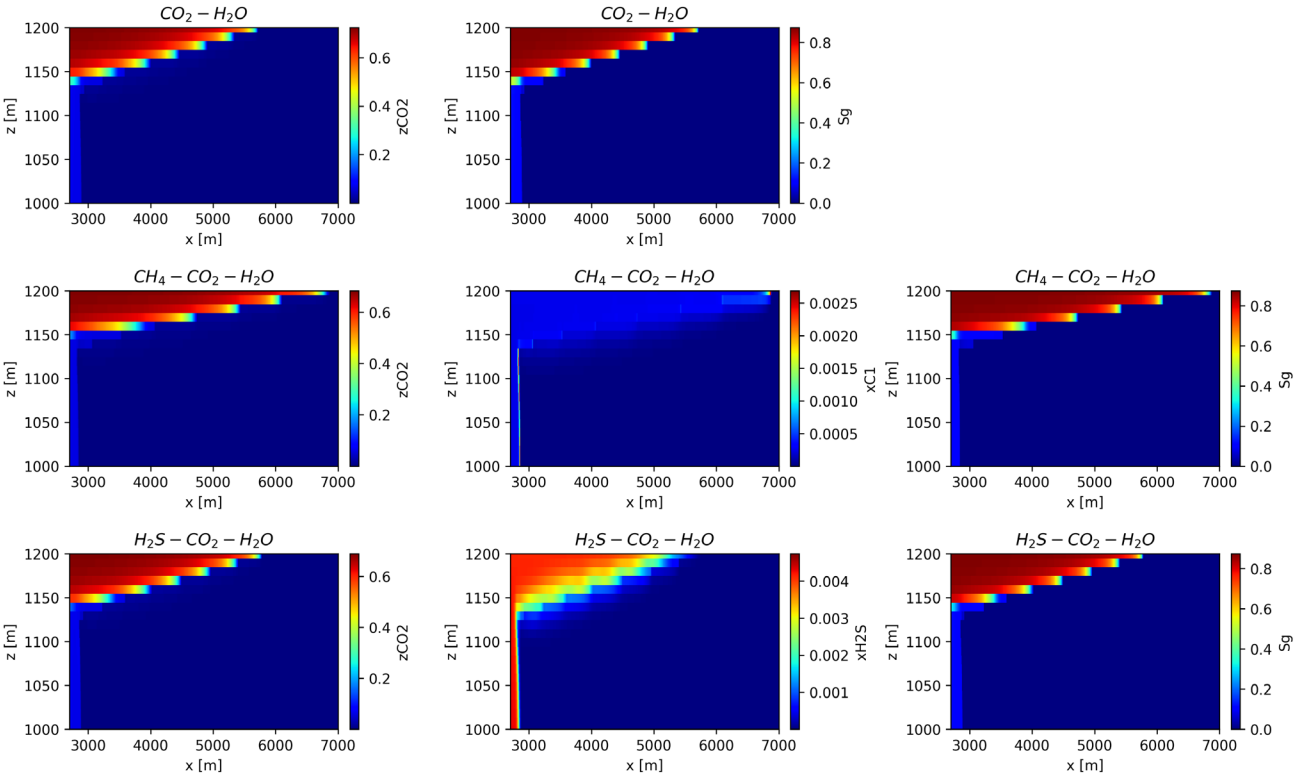


Fig. 14—SPE11b is homogenized to Facies 5 and a 5 mol% CO_2 mixture of H_2S (bottom row) and CH_4 (middle row) is injected and compared to pure CO_2 injection (top row).

higher-resolution models, while non-K-orthogonal grids with multi-point flux approximation (MPFA) discretizations are best reserved for lower-resolution models (Wapperom et al. 2024; Holme et al. 2025). The reasoning for this is twofold: First, the different grids and schemes agree on CO_2 plume dynamics (migration pathways, final position, etc.) and second, grid refinement with TPFA is more effective in terms of computational cost than MPFA approximations for resolving the convective mixing process.

Although cubic EOSs have proved to be reliable for nonpolar mixtures, experimental data have revealed that their predictions of interactions between associating particles are insufficient. In our simulations, a separate EOS is used for the aqueous phase that facilitates the modeling of ternary and quaternary brine/gas mixtures, while maintaining the computational efficiency of cubic EOS. This hybrid-EOS approach introduces inconsistencies in the vicinity of solvent criticality and beyond. However, conditions considered in saline aquifers remain well below the critical conditions of aqueous phases. Of additional consideration for saline aquifers is whether or not CH_4 is

Downloaded from http://onepetro.org/SJ/article-pdf/31/05/3363/5335132/spe-223922-pa.pdf by Bibliotheek TU Delft user on 27 May 2026

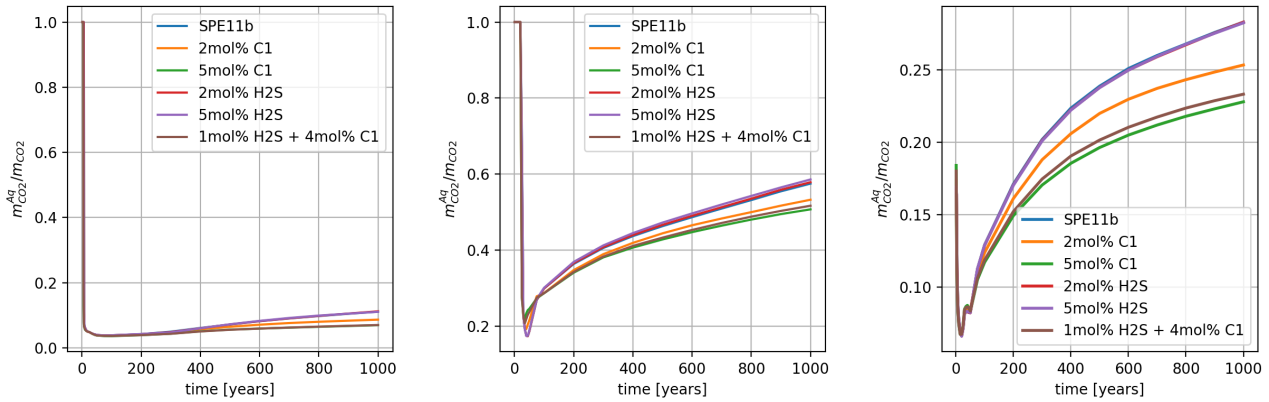


Fig. 15—Comparison of dissolution ratios of CO_2 in the SPE11b with H_2S and CH_4 impurities. From left to right: Box A, Box B, and the entire solution domain.

present in the water before injection. If this is the case, the CH_4 may exsolve from the aqueous phase into the gas and form a more pronounced CH_4 bank at the leading edge of the CO_2 plume.

The findings indicate that while impurities do affect the density and phase behavior of the gas plume, the flow solution of the SPE11b benchmark with H_2S and/or CH_4 impurities closely resembles that of the standard SPE11b model. This finding suggests that trace amounts of these components are unlikely to compromise storage security. However, it is well understood that geochemical interactions with reservoir rocks, particularly in the case of CO_2 and H_2S, are considerable. It is imperative to note that both CO_2 and H_2S are acidic gases. Once dissolved in water, these gases have been shown to decrease the pH level and influence mineral precipitation and dissolution reactions. The CSP does not incorporate geochemistry into its model. However, given the relevance of this matter to caprock integrity and reservoir permeability, it is necessary to understand the geochemistry of the problem before a conclusive assessment can be made of the influence of H_2S on storage security.

Conclusion

The SPE11 benchmark necessarily balances model complexity and usability and therefore makes a number of simplifying assumptions while simultaneously retaining all the necessary physics to capture the three most critical trapping mechanisms for GCS in saline aquifers (solubility-, capillary-, and structural trapping). As such, it includes key physics of CO_2 plume behavior, including the solubility of CO_2 in aquifer water, the buoyancy of gaseous CO_2, diffusion, dispersion, and capillary forces. In this study, the SPE11b and SPE11c benchmark models are simulated using the open-source reservoir simulator open-DARTS and are furthermore subjected to a grid convergence analysis. In all models, it is found that CO_2 is effectively trapped under the capillary barriers, migrates across different units, and dissolves into the aquifer brine. In addition, we assess the effect of CH_4 and/or H_2S impurities in the injection stream on CO_2 plume behavior and storage using a cubic-EOS-based approach of DARTS-flash and find that these impurities have a measurable effect on CO_2 plume behavior.

Evident from all the SPE11 CSP submissions and available literature, differences in grid resolution clearly influence dissolution fingers and convective mixing of CO_2. In the case of the 11b model, a structured mesh is utilized at various resolutions, ranging from approximately 50,000 to 600,000 gridblocks. The results indicate that the solution for the SPE11b benchmark starts to converge with regard to dissolved mobile and immobile CO_2 at a horizontal resolution of 1,340 and a vertical resolution of 240 blocks per dimension (approximately 300,000 grid cells). In contrast to other submissions to the CSP, the incorporation of dispersion has been observed to result in a significant increase in the wavelength of the dissolution fingers. In this paper, we do not provide a comparison with other submissions to the CSP. Accordingly, the reader is referred to the results of the CSP, in which it may be observed that all available timeseries proxies/metrics align with the general trend set by all the submissions (Nordbotten et al. 2025). Furthermore, it is noteworthy that the increase in wavelength due to dispersion indicates that the necessary resolution for a converged solution is less than the critical wavelength equation and diffusion coefficients initially suggested. Therefore, the recommended resolution of 300,000 gridblocks is a reasonable resolution that achieves an acceptable balance between capturing the convective mixing process and runtime. However, implementing this resolution for the 3D SPE11c model would necessitate a model with a cost of up to 80.4 million gridblocks. Consequently, a simulation was conducted on the SPE11c model with a reduced grid resolution of approximately 8 million active gridlocks. This resolution is presumably inadequate for resolving fine-scale convective features associated with solubility trapping.

The predominant consensus among researchers is that achieving a numerically converged solution to the SPE11 benchmark necessitates the utilization of high-resolution and high-performance computing capabilities. In addition, in actual cases, the injected gas stream is predicted to be a mixture of CO_2 and various impurities, depending on the origin of the CO_2. Consequently, it is worthwhile to consider whether the limited degrees of freedom might be repurposed to model injection impurities. In this particular instance, the established benchmark is expanded to include H_2S and CH_4 in the injection stream with molar fractions reaching up to 5 mol%.

From the results, it is observed that CH_4 decreases gas density and thus increases buoyancy, leading to increased lateral spread of the CO_2 plume. Additionally, CH_4 accumulates at the front of the CO_2 plume, highlighting its potential use for CO_2 plume monitoring and improved characterization of the reservoir structure. In terms of CO_2 dissolution, CH_4 is found to reduce solubility trapping significantly: A 5 mol% CH_4 concentration in the injection stream decreases CO_2 dissolution by approximately 5%. Conversely, it is found that H_2S under reservoir conditions increases the density of the CO_2 plume and thus slightly inhibits its spread. In addition, the H_2S simulation demonstrates chromatographic partitioning of CO_2 and H_2S and shows a negligible effect on the solubility trapping of CO_2. Together, these findings highlight the importance of impurity characterization in CCS projects and demonstrate the utility of the hybrid-EOS model in capturing the effects of impurities on CO_2 migration.

Downloaded from http://onepetro.org/SJ/article-pdf/31/05/3363/5335132/spe-223922-pa.pdf by Bibliotheek TU Delft user on 27 May 2026

Data Availability Statement

The models and code are open-source and are available at the open-DARTS repository: https://gitlab.com/open-darts.

Acknowledgments

The authors thank Shell and TotalEnergies for funding this work through the ASSET and FC-MAELSTROM Projects.

References

Bachu, S. and Bennion, D. B. 2009. Chromatographic Partitioning of Impurities Contained in a CO_2 Stream Injected into a Deep Saline Aquifer: Part 1. Effects of Gas Composition and in Situ Conditions. *Int J Greenh Gas Control* **3** (4): 458–467. https://doi.org/10.1016/j.ijggc.2009.01.001.

Bando, S., Takemura, F., Nishio, M. et al. 2004. Viscosity of Aqueous NaCl Solutions with Dissolved CO_2 at (30 to 60) °C and (10 to 20) MPa. *J Chem Eng Data* **49** (5): 1328–1332. https://doi.org/10.1021/je049940f.

Bear, J. and Cheng, A. 2010. *Modeling Groundwater Flow and Contaminant Transport*. Dordrecht, Netherlands: Springer. https://doi.org/10.1007/978-1-4020-6682-5.

Eiken, O., Ringrose, P., Hermanrud, C. et al. 2011. Lessons Learned from 14 Years of CCS Operations: Sleipner, In Salah and Snøhvit. *Energy Procedia* **4**: 5541–5548. https://doi.org/10.1016/j.egypro.2011.02.541.

Elenius, M. T., Voskov, D. V., and Tchelepi, H. A. 2015. Interactions between Gravity Currents and Convective Dissolution. *Adv Water Resour* **83** (77): 77–88. https://doi.org/10.1016/j.advwatres.2015.05.006.

Fenghour, A., Wakeham, W. A., and Vesovic, V. 1998. The Viscosity of Carbon Dioxide. *J Phys Chem Ref Data* **27** (1): 31–44. https://doi.org/10.1063/1.556013.

Flemisch, B., Nordbotten, J. M., Fernø, M. et al. 2024. The FluidFlower Validation Benchmark Study for the Storage of CO_2. *Transp Porous Med* **151** (5): 865–912. https://doi.org/10.1007/s11242-023-01977-7.

Gamal Rezk, M., Farid Ibrahim, A., and Adebayo, A. R. 2023. Influence of Impurities on Reactive Transport of CO_2 during Geo-Sequestration in Saline Aquifers. *Fuel* **344**: 127994. https://doi.org/10.1016/j.fuel.2023.127994.

Garcia, J. E. 2001. Density of Aqueous Solutions of CO_2. Technical Report. Lawrence Berkeley National Laboratory (LBNL), Berkeley, California, USA.

Hajiw, M., Corvisier, J., Ahmar, E. E. et al. 2018. Impact of Impurities on CO_2 Storage in Saline Aquifers: Modelling of Gases Solubility in Water. *Int J Greenh Gas Control* **68**: 247–255. https://doi.org/10.1016/j.ijggc.2017.11.017.

Hnedkovsky, L., Wood, R. H., and Majer, V. 1996. Volumes of Aqueous Solutions of CH_4, CO_2, H_2S and NH_3at Temperatures from 298.15 K to 705 K and Pressures to 35 MPa. *J Chem Thermodyn* **28** (2): 125–142. https://doi.org/10.1006/jcht.1996.0011.

Holme, K., Lie, K.-A., Møyner, O. et al. 2025. Grid-Orientation Effects in the 11th SPE Comparative Solution Project Using Unstructured Grids and Consistent Discretizations. *SPE J.* **30** (10): 6313–6328. https://doi.org/10.2118/223885-PA.

Huang, S. S.-S., Leu, A.-D., Ng, H.-J. et al. 1985. The Phase Behavior of Two Mixtures of Methane, Carbon Dioxide, Hydrogen Sulfide, and Water. *Fluid Phase Equilib* **19** (1–2): 21–32. https://doi.org/10.1016/0378-3812(85)85033-0.

Islam, A. W. and Carlson, E. S. 2012. Viscosity Models and Effects of Dissolved CO_2. *Energy Fuels* **26** (8): 5330–5336. https://doi.org/10.1021/ef3006228.

Khait, M. and Voskov, D. V. 2017. Operator-Based Linearization for General Purpose Reservoir Simulation. *J Pet Sci Eng* **157**: 990–998. https://doi.org/10.1016/j.petrol.2017.08.009.

Khait, M. and Voskov, D. 2021. A GPU-Based Integrated Simulation Framework for Modelling of Complex Subsurface Applications. Paper presented at the SPE Reservoir Simulation Conference, On-Demand, 26 October, 2021. https://doi.org/10.2118/204000-MS.

Koschel, D., Coxam, J.-Y., Rodier, L. et al. 2006. Enthalpy and Solubility Data of CO_2 in Water and NaCl(Aq) at Conditions of Interest for Geological Sequestration. *Fluid Phase Equilib* **247** (1–2): 107–120. https://doi.org/10.1016/j.fluid.2006.06.006.

Kovscek, A. R., Nordbotten, J. M., and Fernø, M. A. 2024. Scaling Up FluidFlower Results for Carbon Dioxide Storage in Geological Media. *Transp Porous Med* **151** (5): 975–1002. https://doi.org/10.1007/s11242-023-02046-9.

Krevor, S., Blunt, M. J., Benson, S. M. et al. 2015. Capillary Trapping for Geologic Carbon Dioxide Storage – From Pore Scale Physics to Field Scale Implications. *Int J Greenh Gas Control* **40**: 221–237. https://doi.org/10.1016/j.ijggc.2015.04.006.

Lemmon, E., Bell, I., Huber, M. et al. 2023. Thermophysical Properties of Fluid Systems. Technical Report. The National Institute of Standards and Technology (NIST), Gaithersburg, Maryland, USA.

Li, Z. and Firoozabadi, A. 2009. Cubic-Plus-Association Equation of State for Water-containing Mixtures: Is "Cross Association" Necessary? *AIChE J* **55** (7): 1803–1813. https://doi.org/10.1002/aic.11784.

Li, D., He, Y., Zhang, H. et al. 2017. A Numerical Study of the Impurity Effects on CO_2 Geological Storage in Layered Formation. *Appl Energy* **199**: 107–120. https://doi.org/10.1016/j.apenergy.2017.04.059.

Lyu, X. and Voskov, D. 2023. Advanced Modeling of Enhanced CO_2 Dissolution Trapping in Saline Aquifers. *Int J Greenh Gas Control* **127**: 103907. https://doi.org/10.1016/j.ijggc.2023.103907.

Lyu, X., Khait, M., and Voskov, D. 2021. Operator-Based Linearization Approach for Modeling of Multiphase Flow with Buoyancy and Capillarity. *SPE J.* **26** (4): 1858–1875. https://doi.org/10.2118/205378-PA.

Metz, B., Davidson, O., and DeConinck, H., eds. 2005. *IPCC Special Report on Carbon Dioxide Capture and Storage*. New York, USA: Cambridge University Press.

Michelsen, M. L. 1982. The Isothermal Flash Problem. Part II. Phase-Split Calculation. *Fluid Phase Equilibria* **9** (1): 21–40. https://doi.org/10.1016/0378-3812(82)85002-4.

Michelsen, M. L. and Mollerup, J. M. 2004. *Thermodynamic Models: Fundamentals & Computational Aspects*. Denmark: Tie-Line Publications Holte.

Neufeld, J. A., Hesse, M. A., Riaz, A. et al. 2010. Convective Dissolution of Carbon Dioxide in Saline Aquifers. *Geophys Res Lett* **37** (22). https://doi.org/10.1029/2010GL044728.

Nordbotten, J. M., Fernø, M., Flemisch, B. et al. 2022. Final Benchmark Description: FluidFlower International Benchmark Study. https://doi.org/10.5281/zenodo.6807102.

Nordbotten, J. M., Ferno, M. A., Flemisch, B. et al. 2024. The 11th Society of Petroleum Engineers Comparative Solution Project: Problem Definition. *SPE J.* **29** (5): 2507–2524. https://doi.org/10.2118/218015-PA.

Nordbotten, J. M., Fernø, M. A., Flemisch, B. et al. 2025. Benchmarking CO_2 Storage Simulations: Results from the 11th Society of Petroleum Engineers Comparative Solution Project. *Int J Greenh Gas Control* **148**: 104519. https://doi.org/10.1016/j.ijggc.2025.104519.

Novikov, A. and Voskov, D. V. 2025. Interpolation Strategies for Complex Thermal-Multiphase-Reactive Modeling With Operator-Based Linearization. Paper presented at the SPE Reservoir Simulation Conference, Galveston, Texas, USA, 25–27 March. https://doi.org/10.2118/223919-MS.

Orr, F. 2007. *Theory of Gas Injection Processes*. Indianapolis, Indiana, USA: Tie-Line Publications.

Downloaded from http://onepetro.org/SJ/article-pdf/31/05/3363/5335132/spe-223922-pa.pdf by Bibliotheek TU Delft user on 27 May 2026

Pau, G. S. H., Bell, J. B., Pruess, K. et al. 2010. High-Resolution Simulation and Characterization of Density-Driven Flow in CO_2 Storage in Saline Aquifers. *Adv Water Resour* **33** (4): 443–455. https://doi.org/10.1016/j.advwatres.2010.01.009.

Peng, D.-Y. and Robinson, D. B. 1976. A New Two-Constant Equation of State. *Ind Eng Chem Fund* **15** (1): 59–64. https://doi.org/10.1021/i160057a011.

Pruess, K. and Nordbotten, J. 2011. Numerical Simulation Studies of the Long-Term Evolution of a CO_2 Plume in a Saline Aquifer with a Sloping Caprock. *Transp Porous Med* **90** (1): 135–151. https://doi.org/10.1007/s11242-011-9729-6.

Pruess, K., García, J., Kovscek, T. et al. 2004. Code Intercomparison Builds Confidence in Numerical Simulation Models for Geologic Disposal of CO_2. *Energy* **29** (9–10): 1431–1444. https://doi.org/10.1016/j.energy.2004.03.077.

Riaz, A., Hesse, M., Tchelepi, H. A. et al. 2006. Onset of Convection in a Gravitationally Unstable Diffusive Boundary Layer in Porous Media. *J Fluid Mech* **548**: 87–111. https://doi.org/10.1017/S0022112005007494.

Ringrose, P. 2020. *How to Store CO_2 Underground: Insights from Early-Mover CCS Projects*. Cham, Switzerland: Springer Nature. https://doi.org/10.1007/978-3-030-33113-9.

Savary, V., Berger, G., Dubois, M. et al. 2012. The Solubility of CO_2+H_2S Mixtures in Water and 2M NaCl at 120°C and Pressures up to 35MPa. *Int J Greenh Gas Control* **10**: 123–133. https://doi.org/10.1016/j.ijggc.2012.05.021.

Spycher, N., Pruess, K., and Ennis-King, J. 2003. CO_2-H_2O Mixtures in the Geological Sequestration of CO_2. I. Assessment and Calculation of Mutual Solubilities from 12 to 100°C and up to 600 Bar. *Geochim Cosmochim Acta* **67** (16): 3015–3031. https://doi.org/10.1016/S0016-7037(03)00273-4.

Tian, X., Wapperom, M., Gunning, J. et al. 2024. A History Matching Study for the FluidFlower Benchmark Project. *Transp Porous Med* **151** (5): 1113–1139. https://doi.org/10.1007/s11242-023-02048-7.

Voskov, D. V. 2017. Operator-Based Linearization Approach for Modeling of Multiphase Multi-Component Flow in Porous Media. *J Comput Phys* **337**: 275–288. https://doi.org/10.1016/j.jcp.2017.02.041.

Voskov, D., Saifullin, I., Novikov, A. et al. 2024. Open Delft Advanced Research Terra Simulator (Open-DARTS). *JOSS* **9** (99): 6737. https://doi.org/10.21105/joss.06737.

Wapperom, M. 2026. *A Thermodynamics-Based Simulation Framework for Modelling of Geological CO_2 Sequestration*. PhD Dissertation, Delft University of Technology, Delft, Netherlands.

Wapperom, M., Tian, X., Novikov, A. et al. 2024. FluidFlower Benchmark: Lessons Learned from the Perspective of Subsurface Simulation. *Transp Porous Med* **151** (5): 1033–1052. https://doi.org/10.1007/s11242-023-01984-8.

Whitson, C. H. and Michelsen, M. L. 1989. The Negative Flash. *Fluid Phase Equilib* **53**: 51–71. https://doi.org/10.1016/0378-3812(89)80072-X.

Whittaker, S., Rostron, B., Khan, D. et al. 2004. IEA GHG Weyburn CO_2 Monitoring and Storage Project Summary Report 2000-2004. Paper presented at the 7th International Conference on Greenhouse Gas Control Technologies, Vancouver, Canada, 5−9 September.

Zaidin, M. F., Valtz, A., Chapoy, A. et al. 2024. Exploring CO_2-H_2S Storage in Deep Saline Aquifers: A Case Study from an Offshore Gas Field in Malaysia. From Lab to Numerical Simulation. Paper presented at the International Petroleum Technology Conference, Dhahran, Saudi Arabia, 12 February, 2024. https://doi.org/10.2523/IPTC-23428-EA.

Zhang, W., Xu, T., and Li, Y. 2011. Modeling of Fate and Transport of Coinjection of H_2S with CO_2 in Deep Saline Formations. *J Geophys Res Solid Earth* **116**. https://doi.org/10.1029/2010JB007652.

Ziabakhsh-Ganji, Z. and Kooi, H. 2012. An Equation of State for Thermodynamic Equilibrium of Gas Mixtures and Brines to Allow Simulation of the Effects of Impurities in Subsurface CO_2 Storage. *Int J Greenh Gas Control* **11**: S21–S34. https://doi.org/10.1016/j.ijggc.2012.07.025.

Appendix A—Thermodynamic Calculations

In this work, a hybrid-EOS approach for multiphase brine mixtures is used. In this approach, components are distributed between an aqueous phase with no effects of salinity and a vapor phase. To solve the system of governing equations for thermodynamic equilibrium, a fugacity-activity model is applied in a negative flash procedure with successive substitution (Michelsen and Mollerup 2004). The objective function of multiphase Gibbs energy is given by

$$G^* = G/RT = \sum_{j=1}^{n_p} \sum_{i=1}^{n_c} n_{ij} \ln \hat{f}_{ij}, \tag{A-1}$$

where n_{ij} is the number of moles of species i in phase j.

The material balance for each component is given as

$$x_{i0} + \sum_{j=1}^{n_p-1} v_j \left(x_{ij} - x_{i0}\right) = z_v \quad i = 1, ..., n_c, \tag{A-2}$$

where phase zero is the reference phase. Mole fractions of each phase must sum to unity, which gives

$$\sum_{i=1}^{n_c} \left(x_{ij} - x_{i0}\right) = 0, \quad j = 1, ..., n_p - 1. \tag{A-3}$$

When calculating phase equilibrium, the material balance and fugacity constraints must be satisfied. The equilibrium equations as given by Michelsen (1982) are

$$\ln y_i - \ln x_i = \ln K_{il} = \ln \phi_i^j - \ln \phi_i^k, \quad l = 1, ..., n_p - 1. \tag{A-4}$$

Because the model utilizes successive substitution, the material balance is solved using the Rachford-Rice equation in an inner loop where fugacity coefficients are considered composition-independent, while fugacities are updated in an outer loop. This weak dependence on composition results in rapid convergence, as shown in Michelsen (1982). In this binary system, the Rachford-Rice equation is a monotonically decreasing function within the negative flash window, so the inner loop can be directly solved. To calculate fugacities for phase equilibrium, the Peng-Robinson EOS (Peng and Robinson 1976) is used for the vapor phase, while an activity model is used for the aqueous phase (Ziabakhsh-Ganji and Kooi 2012).

The activity model has a direct expression in terms of pressure, temperature, and composition to solve for activity and fugacity. For the Peng-Robinson EOS, the partial derivatives of the reduced residual Helmholtz function F:

Downloaded from http://onepetro.org/SJ/article-pdf/31/05/3363/5335132/spe-223922-pa.pdf by Bibliotheek TU Delft user on 27 May 2026

$$F = \frac{A^r\left(T, V, \mathbf{n}\right)}{RT}, \tag{A-5}$$

are used to calculate thermodynamic properties. In this fugacity-activity approach, the fugacity and its derivatives are given as

$$\ln \hat{\varphi}_i = \left(\frac{\partial F}{\partial n_i}\right)_{T,V} - \ln Z, \tag{A-6}$$

$$\left(\frac{\partial \ln \hat{\varphi}_i}{\partial T}\right)_{P,\mathbf{n}} = \left(\frac{\partial^2 F}{\partial T \partial n_i}\right)_{V} + \frac{1}{T} - \frac{\bar{V}_i}{RT}\left(\frac{\partial P}{\partial T}\right)_{V,\mathbf{n}}. \tag{A-7}$$

Properties directly used to capture thermal effects and phase mixing during CO_2 injection include density and enthalpy, the latter of which is given as

$$\frac{\bar{H}_i^r\left(T, P, \mathbf{n}\right)}{RT} = -T\left(\frac{\partial \ln \hat{\varphi}_i}{\partial T}\right)_{P,\mathbf{n}}. \tag{A-8}$$

Using the a and b constants from the Peng-Robinson EOS, the Helmholtz energy for n moles of a mixture is then given by

$$F = \frac{A^r\left(T, V, \mathbf{n}\right)}{RT} = -n\ln\left(1 - B/V\right) - \frac{D\left(T\right)}{RTB\left(\delta_1 - \delta_2\right)}\ln\left(\frac{1 + \delta_1 B/V}{1 + \delta_2 B/V}\right), \tag{A-9}$$

where B denotes nb_{mix} and D denotes $n^2 a_{mix}$ for mixture parameters a_{mix} and b_{mix} that replace pure component parameters a and b from the EOS. Terms δ_1 and δ_2 are given as

$$\delta_1 = \frac{1}{2}\left(c + 1 + \sqrt{\left(c+1\right)^2 + 4c}\right), \tag{A-10}$$

and

$$\delta_2 = \frac{1}{2}\left(c + 1 - \sqrt{\left(c+1\right)^2 + 4c}\right). \tag{A-11}$$

Appendix B—Experimental Data

In this appendix, the results of thermodynamic calculations for a quaternary mixture with composition of 15 mol% of CH_4, 30 mol% of CO_2, 5 mol% of H_2S, and 50 mol% of H_2O are presented next to experimental data points from Huang et al. (1985). The results show good agreement with the experimental data. Additional comparisons, including graphical comparisons with experimental data sets, are included in Wapperom (2026).

		exp	DARTS	exp	DARTS	exp	DARTS	exp	DARTS	exp	DARTS
P (bar)	T (°C)	xC1	xC1	xCO_2	xCO_2	xH_2S	xH_2S	xH_2O	xH_2O	V (%)	V (%)
48.2	37.8	2.76×10^{-4}	2.82×10^{-4}	9.30×10^{-3}	9.84×10^{-3}	5.03×10^{-3}	5.02×10^{-3}	0.9854	0.9849	4.08	4.15
76.0		4.66×10^{-4}	4.26×10^{-4}	1.21×10^{-2}	1.29×10^{-2}	5.40×10^{-3}	6.41×10^{-3}	0.9816	0.9802	7.30	7.45
125.2		7.96×10^{-4}	6.81×10^{-4}	1.51×10^{-2}	1.51×10^{-2}	5.95×10^{-3}	7.09×10^{-3}	0.9781	0.9771	14.5	14.86
169.3		9.90×10^{-4}	8.75×10^{-4}	1.54×10^{-2}	1.57×10^{-2}	6.08×10^{-3}	7.20×10^{-3}	0.9777	0.9762	19.9	19.80
83.6	107.2	3.79×10^{-4}	3.54×10^{-4}	6.98×10^{-3}	7.45×10^{-3}	3.42×10^{-3}	4.52×10^{-3}	0.9894	0.9877	5.38	5.45
129.3		5.78×10^{-4}	5.23×10^{-4}	9.59×10^{-3}	9.99×10^{-3}	4.47×10^{-3}	5.94×10^{-3}	0.9854	0.9835	8.66	8.87
171.7		7.79×10^{-4}	6.68×10^{-4}	1.13×10^{-2}	1.17×10^{-2}	4.73×10^{-3}	6.86×10^{-3}	0.9834	0.9808	11.8	11.94
118.0	176.7	7.17×10^{-4}	6.35×10^{-4}	7.95×10^{-3}	8.70×10^{-3}	3.74×10^{-3}	4.19×10^{-3}	0.9877	0.9865	5.82	5.42
173.1		1.10×10^{-3}	9.19×10^{-4}	1.14×10^{-2}	1.18×10^{-2}	4.78×10^{-3}	5.63×10^{-3}	0.9827	0.9816	8.65	8.43

Table B-1—Aqueous molar phase fraction and relative liquid volumes in the two-phase region vs. experimental data from Huang et al. (1985). Overall composition of mixture: (15 mol% CH_4, 30 mol% CO_2, 5 mol% H_2S, and 50 mol% H_2O). The mean absolute percentage error per component across all the data points is equal to 10.5%, 4.71%, 21.8%, and 0.1456%.

Downloaded from http://onepetro.org/SJ/article-pdf/31/05/3363/5335132/spe-223922-pa.pdf by Bibliotheek TU Delft user on 27 May 2026

		exp	DARTS	exp	DARTS	exp	DARTS	exp	DARTS
P (bar)	*T* (°C)	yC1	yC1	yCO_2	yCO_2	yH_2S	yH_2S	yH_2O	yH_2O
48.2	37.8	0.3040	0.3037	0.5945	0.5979	0.0998	0.0962	0.0019	0.0021
76.0		0.3031	0.3052	0.5970	0.5978	0.0982	0.0952	0.0017	0.0018
125.2		0.3029	0.3058	0.5967	0.5973	0.0985	0.0948	0.0019	0.0020
169.3		0.3021	0.3058	0.5963	0.5970	0.0996	0.0947	0.0020	0.0024
83.6	107.2	0.2907	0.2960	0.5919	0.5854	0.0967	0.0944	0.0225	0.0242
129.3		0.2929	0.2984	0.5920	0.5880	0.0963	0.0938	0.0196	0.0198
171.7		0.2935	0.2996	0.5916	0.5888	0.0970	0.0932	0.0179	0.0185
118.0	176.7	0.2641	0.2681	0.5575	0.5304	0.0848	0.0862	0.0950	0.1152
173.1		0.2762	0.2760	0.5520	0.5435	0.0870	0.0875	0.0848	0.0930

Table B-2—Vapor molar phase fraction in the two-phase region vs. experimental data from Huang et al. (1985). Overall composition of mixture: (15 mol% CH_4, 30 mol% CO_2, 5 mol% H_2S, and 50 mol% H_2O). The mean absolute percentage error per component across all the data points is equal to 1.151%, 1.066%, 2.95%, and 10%.

Downloaded from http://onepetro.org/SJ/article-pdf/31/05/3363/5335132/spe-223922-pa.pdf by Bibliotheek TU Delft user on 27 May 2026